

3rd International Conference on Material and Component Performance
under Variable Amplitude Loading, VAL2015

Computationally-efficient non-linear kinematic models to predict multiaxial stress-strain behavior under variable amplitude loading

Marco Antonio Meggiolaro^{a,*}, Jaime Tupiassú Pinho de Castro^a, Hao Wu^b

^a*Dept. of Mechanical Engineering, Pontifical Catholic University of Rio de Janeiro, Brazil*

^b*School of Aerospace Engineering and Applied Mechanics, Tongji University, Shanghai, P.R. China*

Abstract

The best multiaxial fatigue damage models require the knowledge of both stress and corresponding strain histories to quantify damage. Under variable amplitude (VA) non-proportional (NP) loadings, efficient correlation between multiaxial stresses and strains requires incremental plasticity models including non-linear kinematic (NLK) hardening. In this work, the formulation of the main NLK models is unified in a generalized equation, represented using engineering notation in a reduced-order five-dimensional space that may lower in half the associated computational cost. NP tension-torsion experiments with 316L steel tubular specimens are conducted to validate the proposed approach.

© 2015 The Authors. Published by Elsevier Ltd. This is an open access article under the CC BY-NC-ND license (<http://creativecommons.org/licenses/by-nc-nd/4.0/>).

Peer-review under responsibility of the Czech Society for Mechanics

Keywords: Multiaxial fatigue; Non-proportional loading; Variable amplitude loading; Stress-strain relations; Incremental plasticity.

1. Introduction

The Bauschinger effect, observed under cyclic loading, is a change in the absolute value of the opposite yield strength after strain hardening, due to the microscopic stress distribution. In other words, loading a specimen above its yield limit in one direction reduces (in absolute value) the yield strength in the opposite direction.

For instance, assume the yield surface currently has a radius $S = S_Y$. Tensile cold working up to a stress level $\sigma_{max} > S_Y$ increases the tensile yield strength from S_Y to σ_{max} in the load direction for subsequent cycles, but it also reduces

* Corresponding author. Tel.: +55-21-35271424.

E-mail address: meggi@puc-rio.br

in absolute value the compressive yield strength, from $-S_Y$ to roughly $(\sigma_{\max} - 2S_Y)$, and vice-versa after a compressive strain hardening. This is a general phenomenon found in most polycrystalline metals, the most significant hardening type after the material becomes cyclically stable.

Figure 1 exemplifies the Bauschinger effect for a uniaxial load history represented in the $\sigma_x \times \tau_{xy}\sqrt{3}$ Mises diagram. In this example, the yield surface $\sigma_{\text{Mises}} = S_Y$ is allowed to translate with no change in its shape or radius S . If the center of the yield surface is translated in the x direction of the Mises stress space by $(\sigma_{\max} - S_Y)$, then the resulting surface will intersect the x axis in the new tensile yield stress $(\sigma_{\max} - S_Y + S_Y) = \sigma_{\max}$ and in the new compressive yield stress $(\sigma_{\max} - S_Y - S_Y) = (\sigma_{\max} - 2S_Y)$. Since this phenomenon only involves the kinematic translation of the yield surface, it is called *kinematic hardening*. The new yield surface center is named *backstress*, represented by a vector $\vec{\beta}$, which stores plastic memory. In Fig. 1, β_x is the x component of such backstress.

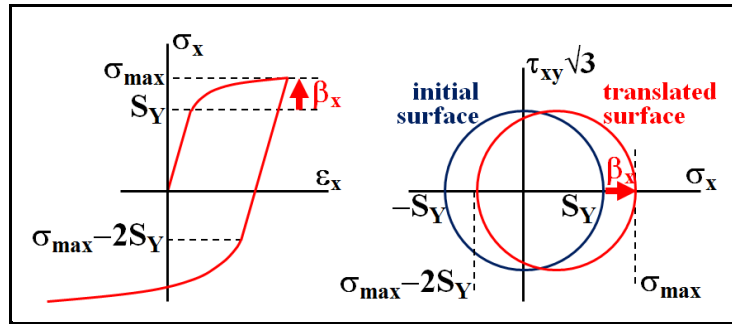


Fig. 1: Kinematic hardening in the x direction and associated yield surface translation in the $\sigma_x \times \tau_{xy}\sqrt{3}$ Mises diagram.

A simple rheological model of the kinematic hardening process has been proposed in [1], as shown in Fig. 2 for uniaxial histories, based on the values of Young's modulus E and a "generalized plastic modulus" C , which describes the slope decrease in the stress-strain curve beyond yielding. The model consists of an elastic spring with stiffness E in series with an inelastic element defined by a spring and a slider in parallel, loaded by a force numerically equal to the stress σ_x . The deformation of the elastic spring is thus the elastic strain $\epsilon_{xe} = \sigma_x/E$, while the plastic strain ϵ_{xp} is associated in this analogy with the deformation of the inelastic element, see Fig. 2(a). The elastic spring from the inelastic element, which has a stiffness C and is loaded by a force numerically equal to the backstrain component β_x , can be interpreted as an elastic strain on the microscale level caused by dislocation-induced lattice deformation [2]. The slider is a Coulomb friction element that only moves when the absolute value of the resulting "force" $(\sigma - \alpha)$ acting on it is large enough to overcome a threshold, the yield stress S_Y .

In a virgin specimen, the backstress component in the x direction is initially $\beta_x = 0$, therefore plastic straining will only happen in traction when $(\sigma_x - \beta_x) = \sigma_x \geq S_Y$, see Fig. 2(a). After reaching a maximum stress $\sigma_{\max} \geq S_Y$, the backstress component has changed from zero to $\beta_x = (\sigma_{\max} - S_Y)$, see Fig. 2(b). During elastic unloading, the slider element will not move until its "force" reaches $-S_Y$, causing reverse yielding. This reverse yielding condition is then given by $(\sigma_x - \beta_x) = \{\sigma_x - (\sigma_{\max} - S_Y)\} \leq -S_Y$, which agrees with the model prediction $\sigma_x \leq \sigma_{\max} - 2S_Y$.

Note that, during plastic straining, as the slider moves, the material stiffness becomes the combination of the springs E and C in series, resulting in the lower slope $EC/(E+C)$, shown in Fig. 2(b). A more precise multi-linear approximation of the stress-strain curve can be obtained if multiple inelastic elements are arranged in parallel, as in the non-linear kinematic (NLK) models. Such NLK models use multiple surfaces that can translate, with the innermost being the yield surface, contained within the remaining hardening surfaces.

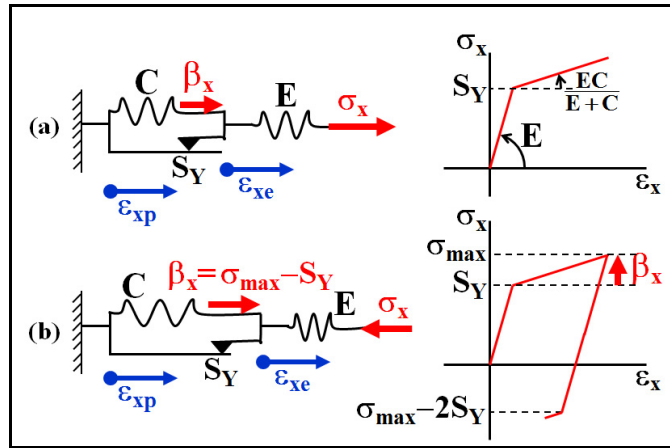


Fig. 2: Uniaxial rheological model for kinematic hardening, showing the (a) elastoplastic loading and (b) elastic unloading process.

A key element of NLK models is the direction in which each yield and hardening surface translates. In uniaxial problems the translation direction is the same as the loading direction, however this is not the case in multiaxial loadings, which in general can have 6 components. In this case, both the backstress vector $\vec{\beta}$ and its incremental translation $d\vec{\beta}$ must be represented in six dimensions (6D). Each NLK model defines a different equation for the 6D direction of such translations. But such directions can be also represented in 5D, without any information loss, using a 5D projection of the stresses, discussed as follows.

2. Five-Dimensional Representation of Stresses and Strains

When dealing with multiaxial stress-strain calculations, it is a good idea to work in stress or strain spaces with reduced dimensions, to save computational effort without modifying the results. By working in the deviatoric space, several equations can be simplified, e.g. Hooke’s law becomes a scalar operation instead of involving multiplications by 9×9 or 6×6 stiffness matrices or their inverse. The 5D Euclidean sub-space E_s , adopted in this work to convert 6D stresses into 5D deviatoric components is:

$$\vec{s}' = \begin{bmatrix} s_1 \\ s_2 \\ s_3 \\ s_4 \\ s_5 \end{bmatrix} = \underbrace{\begin{bmatrix} 1 & -1/2 & -1/2 & 0 & 0 & 0 \\ 0 & \sqrt{3}/2 & -\sqrt{3}/2 & 0 & 0 & 0 \\ 0 & 0 & 0 & \sqrt{3}/2 & 0 & 0 \\ 0 & 0 & 0 & 0 & \sqrt{3}/2 & 0 \\ 0 & 0 & 0 & 0 & 0 & \sqrt{3}/2 \end{bmatrix}}_A \cdot \begin{bmatrix} \sigma_x \\ \sigma_y \\ \sigma_z \\ \tau_{xy} \sqrt{2} \\ \tau_{xz} \sqrt{2} \\ \tau_{yz} \sqrt{2} \end{bmatrix} \quad (1)$$

This sub-space has several useful properties. First, all 6D stresses can be reconstructed from such 5D vector as long as the hydrostatic stress component is known. In addition, this sub-space has a metric based on a von Mises stress, i.e. the absolute value of any 5D component is equal to the von Mises stress at that point. Furthermore, the distance between two 5D stress states becomes the relative von Mises stress between them, a range that is often used in multiaxial damage models such as Sines [3] and Crossland [4].

A similar 5D projection can be defined for strains. Using such 5D stresses and strains, it is possible to calculate stress-strain relations in general multiaxial problems, with a kinematic hardening behavior controlled by the translation rule from the adopted NLK model. The main NLK models are discussed next.

3. Non-Linear Kinematic (NLK) Models

The first non-linear kinematic hardening model was proposed by Armstrong and Frederick in 1966 [5]. Their original single-surface model did not include any additional hardening surface, but their single yield surface already translated according to a non-linear rule. Since then, several improvements on Armstrong-Frederick’s original NLK model have been proposed in the literature.

In the 5D representation, the backstress vector is defined as $\vec{\beta}'$, which locates the center of the yield surface. This vector can be decomposed as the sum of M surface backstresses $\vec{\beta}'_1, \vec{\beta}'_2, \dots, \vec{\beta}'_M$ that describe the relative positions between the centers of consecutive hardening surfaces. In the context of NLK hardening models, such decomposition was proposed by Chaboche et al. [6-7], significantly improving the Armstrong-Frederick model capabilities by indirectly introducing the concept of multiple hardening surfaces.

As mentioned above, the main difference among the several NLK hardening models proposed in the literature rests in the equation of the yield or hardening surface translation direction \vec{v}'_i . In this work, it is shown that most NLK model translations can be condensed into a *unified translation direction*

$$\vec{v}'_i = \underbrace{\vec{n}' \cdot \Delta r_i}_{\text{Prager-Ziegler}} - \chi_i^* \cdot \mathbf{m}_i^* \cdot \gamma_i \cdot \underbrace{[\delta_i \cdot \vec{\beta}'_i + (1 - \delta_i) \cdot (\vec{\beta}'_i{}^T \cdot \vec{n}') \cdot \vec{n}']}_{\text{radial return}} \quad (2)$$

dynamic recovery

where \vec{n}' is the 5D plastic straining direction, Δr_i is the difference between the radii of two consecutive surfaces, and the scalar functions χ_i^* and \mathbf{m}_i^* are defined as

$$\chi_i^* \equiv \left(\frac{|\vec{\beta}'_i|}{\Delta r_i} \right)^{\chi_i} \quad \text{and} \quad \mathbf{m}_i^* \equiv \begin{cases} \left[\frac{\vec{\beta}'_i{}^T \cdot \vec{n}'}{|\vec{\beta}'_i|} \right]^{m_i}, & \text{if } \vec{\beta}'_i{}^T \cdot \vec{n}' \geq 0 \\ \mathbf{0}, & \text{if } \vec{\beta}'_i{}^T \cdot \vec{n}' < 0 \end{cases} \quad (3)$$

The calibration parameters for each yield surface i are the ratcheting exponent χ_i , the multiaxial ratcheting exponent \mathbf{m}_i , the ratcheting coefficient γ_i and the multiaxial ratcheting coefficient δ_i , scalar values that are listed in Table 1 for several popular models.

Table 1: Calibration parameters for the general translation direction from Eq. (2).

Year	Kinematic model	χ_i	\mathbf{m}_i	γ_i	δ_i
1949	Prager [8]	0	0	0	1
1966	Armstrong-Frederick [5]	0	0	$0 \leq \gamma_i \leq 1$	1
1983	Chaboche [7]	1	0	1	1
1986	Burlet-Cailletaud [9]	0	0	$0 \leq \gamma_i \leq 1$	0
1995	Delobelle [10]	0	0	$0 \leq \gamma_i \leq 1$	$0 \leq \delta_i \leq 1$
1996	Jiang-Sehitoglu [11-12]	$0 \leq \chi_i < \infty$	0	1	1
2004	Chen-Jiao [13]	$0 \leq \chi_i < \infty$	1	1	$0 \leq \delta_i \leq 1$
2005	Chen-Jiao-Kim [14]	$0 \leq \chi_i < \infty$	$-\infty < \mathbf{m}_i < \infty$	1	1

The translation direction \vec{v}'_i of each surface from Eq. (2) can be separated into three components: (i) the Prager-Ziegler term, in the normal direction \vec{n}' perpendicular to the yield surface; (ii) the dynamic recovery term, in the opposite direction $-\vec{\beta}'_i$ of the backstress of the considered surface, which acts as a recall term that gradually erases plastic memory with an intensity proportional to the product $\chi_i^* \cdot \mathbf{m}_i^* \cdot \gamma_i \cdot \delta_i$; and (iii) the radial return term, in the opposite direction $-\vec{n}'$ of the normal vector, which affects multiaxial ratcheting predictions, calibrated from the product

$\chi_i^* \cdot \mathbf{m}_i^* \cdot \boldsymbol{\gamma}_i \cdot (\mathbf{1} - \delta_i) \cdot (\bar{\boldsymbol{\beta}}_i^T \cdot \bar{\mathbf{n}}')$. Both dynamic recovery and radial return terms from each surface i are influenced by all four calibration parameters χ_i , \mathbf{m}_i , $\boldsymbol{\gamma}_i$ and δ_i .

Among the models from Table 1, Prager’s [8] translation direction $\bar{\mathbf{v}}'_i = \bar{\mathbf{n}}' \cdot \Delta \mathbf{r}_i$ is not able to predict uniaxial ratcheting since it only uses the Prager-Ziegler term, which is linear. For multiaxial ratcheting, it only predicts a very short transient that almost immediately arrests (shakedown), highly underestimating multiaxial ratcheting rates.

Armstrong and Frederick proposed the use of a ratcheting coefficient $0 \leq \boldsymbol{\gamma}_i \leq \mathbf{1}$, originally intended to be a scalar function of the plastic strain path, including non-linearity in their hardening model [5]. However, in many practical implementations, $\boldsymbol{\gamma}_i$ was assumed as a constant, turning their translation equation $\bar{\mathbf{v}}'_i = \bar{\mathbf{n}}' \cdot \Delta \mathbf{r}_i - \boldsymbol{\gamma}_i \cdot \bar{\boldsymbol{\beta}}'_i$ into a linear rule that suffers the same drawbacks of linear hardening models, with a large overestimation of both uniaxial and multiaxial ratcheting. Even though $\boldsymbol{\gamma}_i$ can calibrate ratcheting rates, with the limit values $\boldsymbol{\gamma}_i = \mathbf{0}$ (Prager’s rule) for no ratcheting and $\boldsymbol{\gamma}_i = \mathbf{1}$ for large ratcheting rates, the linearity associated with a constant $\boldsymbol{\gamma}_i$ makes it impossible to predict multiaxial ratcheting rate decay and arrest (shakedown) observed in several constant amplitude experiments.

Chaboche replaced the constant ratcheting coefficient $\boldsymbol{\gamma}_i$ with the ratio $|\bar{\boldsymbol{\beta}}'_i|/\Delta \mathbf{r}_i$, which ranges from $\mathbf{0}$ in the unhardened condition to $\mathbf{1}$ at saturation, eliminating the discontinuity problem caused by $\boldsymbol{\gamma}_i \neq \mathbf{1}$ [6]. However, even though the resulting surface translation rule $\bar{\mathbf{v}}'_i = \bar{\mathbf{n}}' \cdot \Delta \mathbf{r}_i - (|\bar{\boldsymbol{\beta}}'_i|/\Delta \mathbf{r}_i) \cdot \bar{\boldsymbol{\beta}}'_i$ is an improvement over the constant $\boldsymbol{\gamma}_i$ models such as most implementations of Armstrong-Frederick, it is unable to predict multiaxial ratcheting rate decay and arrest. This model predicts a short ratcheting transient followed by a constant ratcheting rate that never decays, overestimating its effects in multiaxial experiments.

Burlet and Cailletaud noticed that multiaxial experiments generally show lower ratcheting rates than the uniaxial ones for equivalent conditions on stress or strain amplitudes [9]. To lower the multiaxial ratcheting rate predictions without altering the uniaxial response, they replaced the dynamic recovery term with a radial return term, which results in the surface translation direction

$$\bar{\mathbf{v}}'_i = \bar{\mathbf{n}}' \cdot \Delta \mathbf{r}_i - \boldsymbol{\gamma}_i \cdot (\bar{\boldsymbol{\beta}}_i^T \cdot \bar{\mathbf{n}}') \cdot \bar{\mathbf{n}}' \tag{4}$$

Jiang and Sehitoglu [11-12] proposed the translation rule

$$\bar{\mathbf{v}}'_i = \bar{\mathbf{n}}' \cdot \Delta \mathbf{r}_i - (|\bar{\boldsymbol{\beta}}'_i|/\Delta \mathbf{r}_i)^{\chi_i} \cdot \bar{\boldsymbol{\beta}}'_i \tag{5}$$

where $0 \leq \chi_i < \infty$. Jiang-Sehitoglu’s equation becomes a generalized version of Chaboche’s original model [6], which would be obtained for the particular case $\chi_i = \mathbf{1}$. Multiaxial ratcheting rate decay can be predicted, if a ratcheting rate exponent $\chi_i \neq \mathbf{1}$ is chosen in the calibration.

Furthermore, other translation rules are also represented in Table 1, proposed in [13-14], showing that such unified rule is very versatile. In the next section, Eq. (2) is used to predict the tension-torsion elastoplastic behavior of 316L stainless steel specimens, to show the accuracy of the proposed unified translation direction.

4. Experimental Results

To verify the prediction capabilities of the presented unified translation model, tension-torsion experiments are performed on annealed tubular 316L stainless steel specimens in an MTS 809.25 multiaxial testing machine, shown in Fig. 3. Engineering stresses and strains are calculated from load/torque cell measurements and from an MTS 632.68 axial/torsional extensometer, and then converted to true stresses and strains.

The engineering shear stresses include the elastoplastic gradient correction recommended by ASTM E2207-08 [15], otherwise they could be overestimated by 10% or more. In this correction, instead of assuming elastic conditions across the tubular specimen wall, ASTM E2207-08 adopts a uniformly-distributed shear stress given by

$$\tau_{ASTM}^{eng} \equiv \frac{16 \cdot T}{\pi \cdot (d_{ext}^2 - d_{int}^2) \cdot (d_{ext} + d_{int})} \tag{6}$$

where \mathbf{T} is the applied torque, and d_{ext} and d_{int} are the specimen outer and inner diameters at the critical section.

The tests consist of strain-controlled tension-torsion load cycles applied to the tubular specimens shown in Fig. 4, until the material cyclically stabilizes, for non-proportional constant and variable amplitude loadings. Non-proportional hardening is modeled using Tanaka's polarization tensor approach [16], adopting an additional hardening coefficient $\alpha_{\text{NP}} = 0.8$, typical of 316L steel values in room temperature under the maximum adopted stress levels. Figure 5 shows an experiment for normal strain amplitudes $\Delta\epsilon_x/2$ and effective shear strain amplitudes $\Delta\gamma_{xy}/(2\sqrt{3})$ varying from 0.2% to 0.8%, following a non-proportional path that describes a square in the $\epsilon_x \times \gamma_{xy}/\sqrt{3}$ strain diagram, where only the 0.2% and 0.8% amplitude cycles are plotted for clarity.



Fig. 3: Tension-torsion testing machine and extensometer.

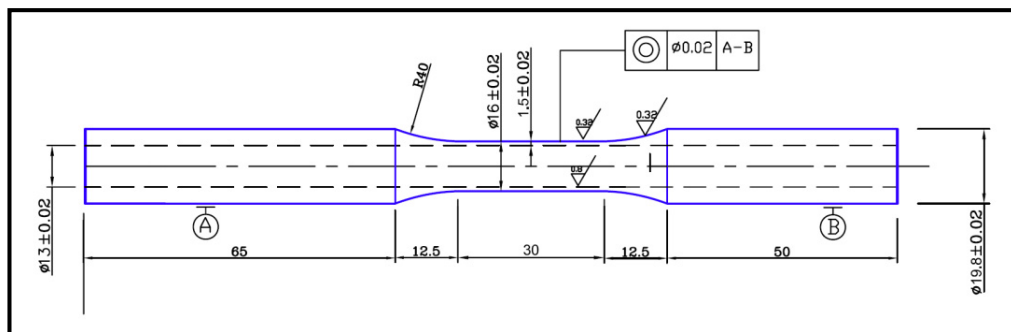


Fig. 4: Typical tubular specimen used in the multiaxial tension-torsion experiments. Normal and shear strains are usually measured by a special clip-gage. For experiments involving large compression strains, the minimum wall thickness is sometimes increased from 1.5 to 2.0 or even 2.5mm to avoid buckling.

The stress paths predicted by the presented incremental plasticity approach for Jiang-Sehitoglu's model, shown in the $\sigma_x \times \tau_{xy}/\sqrt{3}$ stress diagram from Fig. 5, have a very good agreement with the experimentally measured values. Note however that the stress-level dependence of α_{NP} discussed in [17] was confirmed, requiring a lower $\alpha_{\text{NP}} = 0.5$ (instead

of **0.8**) for the lower **0.2%** normal strain amplitudes. It was found that α_{NP} monotonically increased from **0.5** to **0.8** for stabilized non-proportional hysteresis loops with normal amplitudes varying from **0.2%** to **0.8%**.

Figure 6 shows the same paths from Fig. 5 but represented as stress-strain hysteresis loops, both for normal and shear components. Note that the almost vertical portions of the $\sigma_x \times \epsilon_x$ normal hysteresis loops in the left figure represent the torsion cycles, while the almost vertical portion in the shear loops on the right represent the tension-compression cycles.

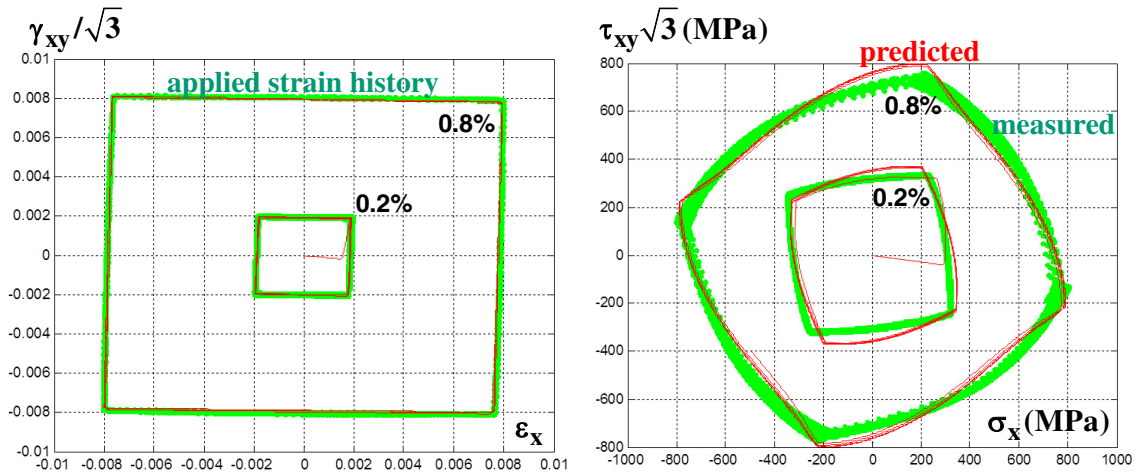


Fig. 5: Square normal-shear strain input path from tension-torsion loads, and resulting normal-shear stress path.

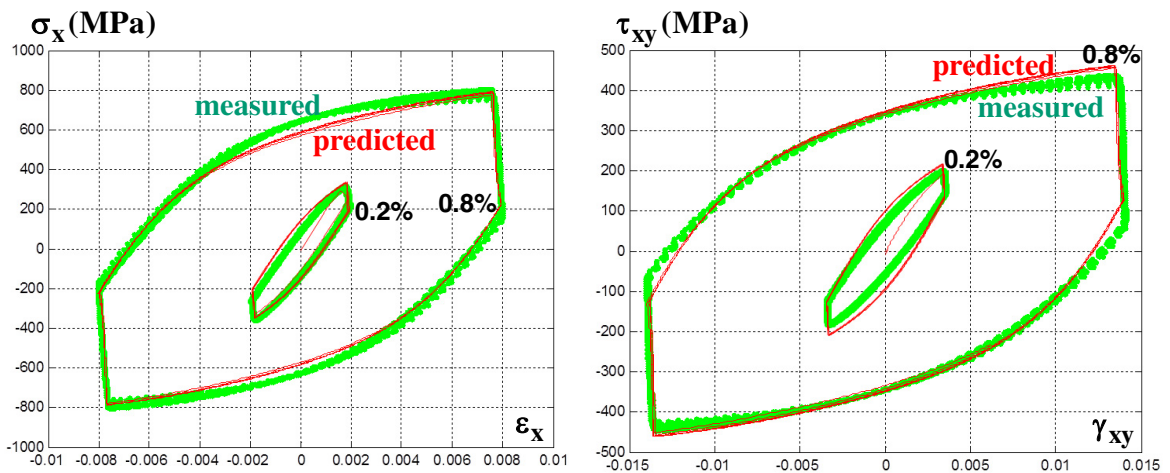


Fig. 6: Stress-strain hysteresis loops associated with the Fig. 5 loading.

From the simulations using the several surface translation rules modeled in Eq. (2), it is found that all rules with adjustable χ_i , γ_i , \mathbf{m}_i , or \mathbf{d}_i allow the calibration of multiaxial ratcheting rates, but the ability to predict both constant rate and rate decay requires either χ_i or δ_i . Moreover, rules with at least two adjustable χ_i , γ_i , \mathbf{m}_i , or \mathbf{d}_i allow independent calibration of uniaxial and multiaxial ratcheting rates. Table 2 summarizes the capabilities of each kinematic hardening translation model that can be represented by the unified Eq. (2), regarding the ability to accurately reproduce uniaxial ratcheting conditions including rate decay, or multiaxial ratcheting conditions with constant rate or with rate decay. Their ability to calibrate arbitrary uniaxial or multiaxial ratcheting rates, as well as to independently calibrate arbitrary uniaxial and multiaxial ratcheting rates, is also evaluated. These models can be readily used to predict the stress-strain behavior in variable-amplitude non-proportional loading histories.

Table 2: Characteristics of the various NLK surface translation direction equations regarding number of parameters to be calibrated (NPC) for **M** surfaces and ability to accurately model all uniaxial ratcheting conditions including rate decay (UR), or all multiaxial ratcheting conditions with constant rate (MRC) or with rate decay (MRD), to calibrate arbitrary uniaxial (U) or multiaxial ratcheting rates (M), and to independently calibrate arbitrary uniaxial and multiaxial ratcheting rates (UM).

Year	Kinematic model	NPC	UR	MRC	MRD	U	M	UM
1949	Prager [8]	0	No	No	No	No	No	No
1966	Armstrong-Frederick [5]	M	No	Yes	No	Yes	Yes	No
1983	Chaboche [7]	0	No	Yes	No	No	No	No
1986	Burlet-Cailletaud [9]	M	No	No	Yes	Yes	Yes	No
1995	Delobelle [10]	2M	No	Yes	Yes	Yes	Yes	Yes
1996	Jiang-Sehitoglu [11-12]	M	Yes	Yes	Yes	Yes	Yes	No
2004	Chen-Jiao [13]	2M	Yes	Yes	Yes	Yes	Yes	Yes
2005	Chen-Jiao-Kim [14]	2M	Yes	Yes	Yes	Yes	Yes	Yes

5. Conclusions

In this work, the formulation of the main non-linear kinematic models was unified in a generalized equation, which describes the translation direction of yield and hardening surfaces in a five-dimensional (5D) deviatoric space. The use of a 5D formulation instead of 6D was able to lower in about half the associated computational cost of the predictions. Non-proportional constant and variable amplitude tension-torsion experiments with 316L steel tubular specimens were conducted to validate the proposed approach, showing good multiaxial stress-strain predictions based on uniaxial material properties, the unified translation rule, and Tanaka's non-proportional hardening model. Conclusions about the abilities of each kinematic hardening rule represented by the unified equation to model uniaxial and multiaxial ratcheting were also evaluated.

References

- [1] Martin, J.F., Topper, T.H., Sinclair, G.M., "Computer Based Simulation of Cyclic Stress-Strain Behavior with Applications to Fatigue," *Materials Research and Standards* v.11(2), p.23-29, ASTM, 1971.
- [2] Lion, A., "Constitutive modelling in finite thermoviscoplasticity: a physical approach based on nonlinear rheological models," *International Journal of Plasticity* v.16, p.469-494, 2000.
- [3] Sines, G. "Behavior of metals under complex static and alternating stresses," in *Metal Fatigue*, p.145-169, McGraw-Hill 1959.
- [4] Crossland B., "Effect of large hydrostatic pressures on the torsional fatigue strength of an alloy steel," In: *Proceedings of International Conference on Fatigue of Metals*. London: IMechE, p.138-149, 1956.
- [5] Armstrong, P.J., Frederick, C.O., "A mathematical representation of the multiaxial Bauschinger effect," CEGB Report RD/B/N731, Berkeley Nuclear Laboratory, 1966.
- [6] Chaboche, J.L., Dang Van, K., Cocard, G., "Modelization of the Strain Memory Effect on the Cyclic Hardening of 316 Stainless Steel," *Transactions of the Fifth International Conference on Structural Mechanics in Reactor Technology*, Div. L, Berlin, 1979.
- [7] Chaboche, J.L., Rousselier, G., "On the Plastic and Viscoplastic Constitutive Equations - Part I: Rules Developed With Internal Variable Concept," *Journal of Pressure Vessel Technology* v.105(2), p.153-158, 1983.
- [8] Prager, W., "Recent developments in the mathematical theory of plasticity," *Journal of Applied Physics* v.20(3), p.235-241, 1949.
- [9] Burlet, H., Cailletaud, G., "Numerical techniques for cyclic plasticity at variable temperature," *Engineering Computations* v.3(2), p.143-153, 1986.
- [10] Delobelle, P., Robinet, P., Bocher, L., "Experimental Study and Phenomenological Modelization of Ratchet under Uniaxial and Biaxial Loading on an Austenitic Stainless Steel," *International Journal of Plasticity* v.11, p.295-330, 1995.
- [11] Jiang, Y., Sehitoglu, H., "Modeling of Cyclic Ratchetting Plasticity, Part I: Development of Constitutive Relations," *ASME Journal of Applied Mechanics* v.63(3), p.720-725, 1996.
- [12] Jiang, Y., Sehitoglu, H., "Modeling of Cyclic Ratchetting Plasticity, Part II: Comparison of Model Simulations with Experiments," *ASME Journal of Applied Mechanics* v.63(3), p.726-733, 1996.
- [13] Chen, X., Jiao, R., "Modified kinematic hardening rule for multiaxial ratcheting prediction," *International Journal of Plasticity* v.20, p.871-898, 2004.
- [14] Chen, X., Jiao, R., Kim, K.S., "On the Ohno-Wang Kinematic Hardening Rules for Multiaxial Ratcheting Modeling of Medium Carbon Steel," *International Journal of Plasticity* v.21, p.161-184, 2005.
- [15] ASTM E2207-08, *Standard Practice for Strain-Controlled Axial-Torsional Fatigue Testing with Thin-Walled Tubular Specimens*, 2013.
- [16] Tanaka, E., "A nonproportionality parameter and a cyclic viscoplastic constitutive model taking into account amplitude dependences and memory effects of isotropic hardening," *European Journal of Mechanics - A/Solids* v.13, p.155-173, 1994.
- [17] Shamsaei, N.; Fatemi, A., "Effect of microstructure and hardness on non-proportional cyclic hardening coefficient and predictions," *Materials Science and Engineering A* 527, p.3015-3024, 2010.